Journal of MATERIALS RESEARCH

Invited Paper
DOI:10.1557/s43578-021-00261-y

MULTISCALE MATERIALS MODELING OF INTERFACE-MEDIATED THERMOMECHANICAL BEHAVIOR

FOCUS ISSUE

Effect of interface structure on dislocation glide behavior in nanolaminates

Wu-Rong Jian[1,a], Yanqing Su[2], Shuozhi Xu[1], Weisen Ji[3], Irene J. Beyerlein[1,4]

[1] Department of Mechanical Engineering, University of California, Santa Barbara, CA 93106-5070, USA
[2] Department of Mechanical and Aerospace Engineering, Utah State University, Logan, UT 84322-4130, USA
[3] Department of Materials Science and Engineering, University of California, Berkeley, CA 94720-1760, USA
[4] Materials Department, University of California, Santa Barbara, CA 93106-5050, USA
[a] Address all correspondence to this author. e-mail: wurong@ucsb.edu

Received: 6 February 2021; accepted: 25 May 2021; published online: 4 June 2021

Irene J. Beyerlein was an editor of this journal during the review and decision stage. For the JMR policy on review and publication of manuscripts authored by editors, please refer to http://www.mrs.org/editor-manuscripts/.

The ultra-high strength of nanolaminates arises from the effect of the fine layering on dislocation motion. Using atomistic simulations, we investigate the effect of the interface structure on the behavior of an edge dislocation driven to glide within a nanolayer of a nanolaminate. Three classes of interface structures are studied, including Cu/Nb or Cu/Cu incoherent interfaces and Nb/Nb coherent interface. Glide behavior is jerky when the interface is incoherent and composed of discrete misfit dislocation arrays. The resistance to glide is non-uniform among parallel glide planes, where planes with intersection lines coinciding with misfit dislocation lines experience greater resistances than those that do not. Interfaces containing misfit dislocations, which extend from the interface into a glide plane in the layer, severely obstruct glide, causing the dislocation to transfer to a parallel plane. Coherent interfaces, while posing the least resistance to initiate and promote smooth glide, lead to strain hardening.

Introduction

Nanolaminated materials have been attracting increasing attention due to their ultra-high strength and unusually stable response to mechanical deformation [1–3], irradiation [4–6], elevated temperatures [7], energy storage [8], and magnetic fields [9, 10]. Many of the more fundamental studies have elected to study bimetal Cu-based nanolaminates as representative nanolaminated materials, such as Cu/V [11], Cu/Nb [12], Cu/W [13], Cu/Ag [14], and Cu/Mo [15] nanolaminates. The mechanical properties of these nanolaminates depend strongly on the properties of the bimetal interfaces that join adjoining layers. When the nanolaminate is strained, these interfaces play multiple roles, acting as barriers to dislocation glide and sites for dislocation reactions and nucleation [16, 17]. Interfaces can be categorized by their atomic structure as being either coherent, semi-coherent, or incoherent interfaces [18]. Some incoherent interfaces can be described by regular arrays of discrete misfit dislocations with distinct Burgers vectors [19–21]. They may also contain regularly occurring atomic steps or facets of lengths and heights and crystallography, which are associated with particular arrays of interfacial dislocations [22, 23]. With atomic scale or analytical modeling, these structural features have been shown to affect the activities of point defects, dislocations, and twins near the interfaces [2, 22, 24–27], the shear strength of the interface [28–30], and mechanical properties [16, 31, 32].

The dimensions of the individual layer thickness L in the nanolaminate can affect the way dislocations move in the layer. In particular, for the range of L commonly occurring in most nanolaminates, 5 nm $< L <$ 100 nm, the dislocations have been proposed and seen to move by confined layer slip (CLS) [33–36]. In CLS, the dislocation segment is confined to glide within a thin nanoscale layer of thickness L, commonly only an order of magnitude greater than the size of its core. The dislocation experiences greater resistance where it joins with the two bounding interfaces than in the interior of the layer, and as such, it bows out as it glides. The resistance associated with overcoming line tension scales as $\ln(L)/L$ [37–39]. Recent CLS models have been extended to include a separate contribution arising from

the interaction between the interface and interface properties [40–42]. However, to date, the contributions of interface structure to CLS have not been thoroughly investigated.

In this work, we utilize molecular dynamics (MD) simulations to investigate the effects of interface structure on the dynamics of and resistance to CLS in nanolaminates of face-centered cubic (FCC) Cu and body-centered cubic (BCC) Nb. The Cu/Nb nanolaminate produced via bulk forming methods is selected as a model material. Since it can be made in sufficient sizes suitable for most tests, it has been the focus of several studies and shown to exhibit excellent structural properties [40, 41, 43, 44], shock resistance [32, 45, 46], and high damage tolerance to ion irradiation [47, 48]. To further highlight the effect of interface structure, we also repeat calculations of confined glide behavior in Cu/Cu and Nb/Nb nanolaminates. The interfaces in the Cu/Nb, Cu/Cu, and Nb/Nb nanolaminates are an incoherent {112} Kurdjumov–Sachs (KS) interface, a symmetric incoherent twin boundary (SITB), and a coherent twin boundary (CTB), respectively. Last, to elucidate the effect of a solid interface, we include baseline calculations of glide in Cu and Nb thin films with the same thickness as the nanolaminates, and in the bulk single crystal of Cu and Nb.

Results

Interface structure and energy

Following the procedure in the Methodology section, four nanolaminate models are built, all with the same individual layer thickness of $L = 5$ nm. The first two are single-phase materials, where one is a Cu/Cu nanolaminate with a {112} SITB and the other is an Nb/Nb nanolaminate with a {112} CTB. The remaining two are Cu/Nb nanolaminates with {112} KS interfaces, one with a central Cu layer and another with a central Nb layer. The relaxed equilibrium atomic structures of these interfaces are shown in Fig. 1. The Cu/Cu SITBs and Cu/Nb {112} KS interface contain a network of misfit (or interfacial) dislocations, which have been characterized in detail in Refs. [27, 49]. The Cu/Cu SITB has an alternating pattern of two parallel arrays, oriented along the $[1\bar{1}0]$ direction, with Burgers vectors b_1 and $-2b_1$ on every (111) plane, where b_1 is a Shockley partial dislocation [49]. The misfit b_1 dislocation extends from the interface an intrinsic stacking fault (ISF) about 5 Å long on a {111} glide plane in Cu. The Cu/Nb {112} KS interface contains three misfit dislocation arrays, with Burgers vectors b_1, b_2, and b_3 [27]. The line orientations of the b_1 and b2 arrays are parallel and aligned along the FCC$[1\bar{1}0]$||BCC$[11\bar{1}]$ axis, while that of the b_3 array is oriented normal to them, directed along FCC$[111]$||BCC$[1\bar{1}0]$. The b_1 misfit dislocation is an edge-type Shockley partial dislocation, with its Burgers vector directed normal to the plane. Due to the low ISF energy of Cu, b_1 extends an ISF about 9 Å in length into the Cu layer. The Burgers vectors b_2 and b_3 line in the plane of the interface, where b_2 is a Frank partial $(a_{Cu}/3)<111>$ and b_3 is a full dislocation. This interface is also faceted with alternating terrace FCC{111}||BCC{110} and FCC{001}||BCC{110} planes. In contrast, the Nb/Nb CTB is, by definition, atomically flat and lacking misfit dislocations.

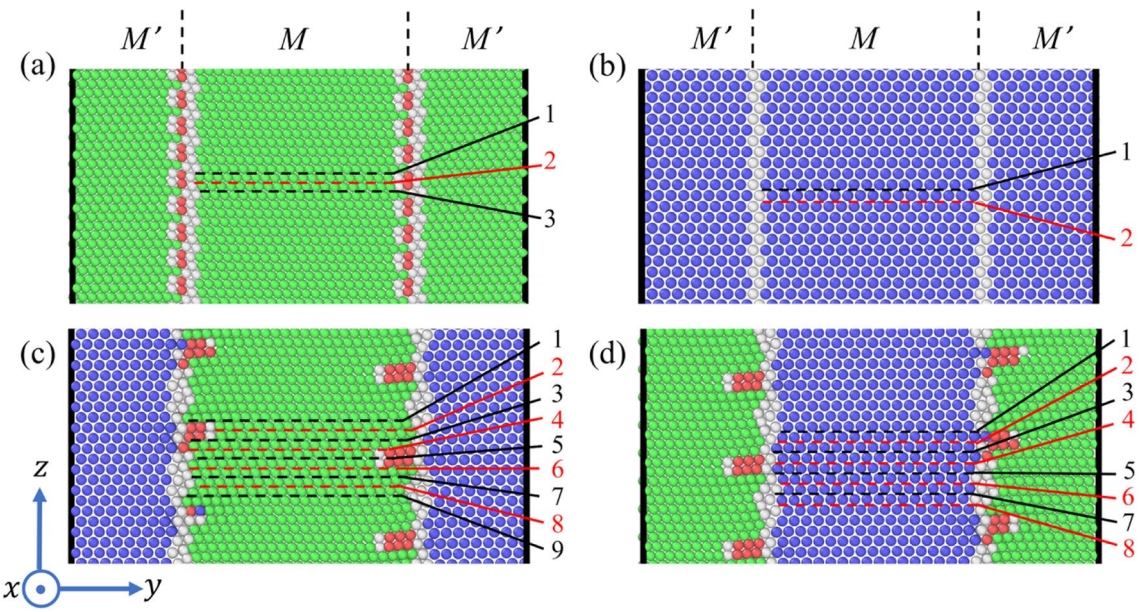

Figure 1: The atomic configurations of (a) Cu/Cu, (b) Nb/Nb, (c) Cu/Nb, and (d) Nb/Cu nanolaminate systems. FCC, BCC, HCP atoms and those with unknown coordination structure are colored by green, blue, red, and gray, respectively. The glide planes in which dislocations could glide in the central *M* layer are indicated by the dashed lines and distinguished by numbers. *M* and *M′* denote neighboring layers of distinct orientations and, in some cases, dissimilar materials as well.

The interfacial energies of the three interfaces are listed in Table 1. The interface energy of the SITB in the Cu/Cu nanolaminate is 467.8 mJ/m^2, lower than the previously reported values (591.9 mJ/m^2 [50] and 590 mJ/m^2 [49]) calculated by the same potential. The differences can arise from the choices made on the number of rigid body translations (RBTs) and cutoff distances used. For example, in Ref. [50], the number of RBTs was 14 and of cutoff distances 172. Here, we used a larger number of RBTs of 100 but a smaller number of cutoff distances of 6. In comparison, the density function theory (DFT) SITB energy in Cu is 630 mJ/m^2 [51]. Our work predicts that the CTB energy in Nb is 137.4 mJ/m^2, while the DFT result is 250 mJ/m^2 [51]. Note that DFT calculations in Ref. [51] attempted approximately 100 RBTs but with only one cutoff distance, for each grain boundary. The {112} KS interface energy of Cu/Nb nanolaminate in our calculations is 822.3 mJ/m^2, consistent with the values (820 to 897 mJ/m^2) in the previous works [27, 52], which used a different potential [53].

Glide planes

After obtaining the interface structure with the lowest interface energy, a perfect edge dislocation with Burgers vector **b** is inserted in grain *M*, as shown in Fig. 8. The method for inserting the edge dislocation depends on whether the layer is Cu or Nb. For the dislocation in the Cu layer, $\mathbf{b} = (a_0/2)\langle 110 \rangle$, while in the Nb layer $\mathbf{b} = (a_0/2)\langle 111 \rangle$, where a_0 is the corresponding lattice parameter of Cu or Nb. The Cu dislocation is introduced by deleting two $(1\bar{1}0)$ atomic planes and the Nb dislocation by deleting three $(11\bar{1})$ atomic planes. After insertion, the system energy is minimized again, which causes the $(a_0/2)[1\bar{1}0]$ dislocation in Cu to dissociate into two 60° Shockley partials with Burgers vectors $(a_0/6)[1\bar{2}1]$ and $(a_0/6)[2\bar{1}\bar{1}]$, respectively. In contrast, the $(a_0/2)[11\bar{1}]$ dislocation in Nb does not dissociate [54, 55]. Then the stress–strain responses are calculated using the methods described in the Methodology section.

The many parallel glide planes, lying within the layers, while being crystallographically equivalent, are not equal in their relationship with the misfit dislocations lying in the interfaces that bound the layers. For the Cu SITB in the Cu/Cu nanolaminate, the periodic unit spans three glide planes in Cu, as shown in Fig. 1a. We use Cu1, Cu2, and Cu3 to denote these planes. All glide planes intersect the Cu/Cu SITB interface along a line that coincides with the line of a misfit dislocation. We refer to these glide planes hereinafter as misfit glide planes. The calculations for CLS are repeated for all three planes. Likewise, for the {112} KS interface in the Cu/Nb nanolaminate, the atomic structure repeats every nine planes in Cu and eight planes in Nb. Among the three different misfit dislocation arrays in this interface, two of them, the b_1 and b_2 arrays, are oriented along the FCC$[1\bar{1}0]$||BCC$[11\bar{1}]$ axis and, thus, share a line of intersection with two glide planes in both Cu and Nb. No plane has a line of intersection with the interface that is aligned with b_3. The nine {111} planes in Cu within the repeating unit of the interface are denoted by Cu1Nb, Cu2Nb, …, and Cu9Nb. Likewise, the eight $\{1\bar{1}0\}$ planes spanning the interface periodic unit are designated by Nb1Cu, Nb2Cu, …, and Nb8Cu. As shown in Fig. 1c, the two misfit glide planes in Cu are Cu5Nb and Cu9Nb, coinciding with b_1 and b_2, respectively. As seen in Fig. 1d, the two misfit glide planes in Nb for these same misfit dislocations are Nb3Cu and Nb6Cu.

Following the procedure described in the Methodology section, four additional models are built: a dislocation gliding in a single crystal in Cu and Nb, denoted as SC-Cu and SC-Nb, respectively, and a dislocation gliding between two {112} free surfaces in Cu and Nb, designated as FS-Cu and FS-Nb, respectively. In each model, the glide of an edge dislocation on only one slip plane is simulated, since all planes are equivalent with respect to the atomic structure of their surroundings.

TABLE 1: Interfacial energies (in mJ/m^2) of the three interfaces in Fig. 1.

Cu/Cu	Nb/Nb	Cu/Nb
467.8	137.4	822.3

Confined layer slip

Cu/Cu nanolaminate

Figure 2a compares the shear stress–strain curves associated with the glide of dislocations on planes Cu1, Cu2, and Cu3 in the Cu/Cu nanolaminate, as well as in the reference cases, SC-Cu and FS-Cu. It is observed that the stresses to move the dislocations are strongly dependent on the glide plane. Among them, CLS on planes Cu1 and Cu3 have similar stress responses, characterized by stress fluctuations around zero (Fig. 2b) over the entire straining period. In the early stages of straining, the stress amplitudes in Cu3 are approximately 41 MPa, but as straining proceeds to the strain of 0.012, they reduce to 8 MPa. Similarly, the stress amplitudes in Cu1 are initially 22 MPa but eventually reduce to 12 MPa at a strain of 0.009. The peak stress for CLS on plane Cu2 is notably six to ten times greater than that for the other two glide planes. The Cu2 response involves a long period of straining where the stress rises continually to a peak value of 278 MPa, after which it drops rapidly before rising again.

Next, we analyzed the behavior of the dislocations corresponding to these three stress–strain responses. Dislocations on all planes begin to move when the first-peak stress is reached, 41 MPa for Cu3, 22 MPa for Cu1, and 278 MPa for Cu2. With continued straining, the motion is oscillatory, meaning the dislocation moves repeatedly forwards and backwards. As an example, the oscillatory dislocation motion in the Cu2 plane is shown in Fig. S1 in the supplementary material. In each oscillation cycle, the forward displacement is far greater than the backward

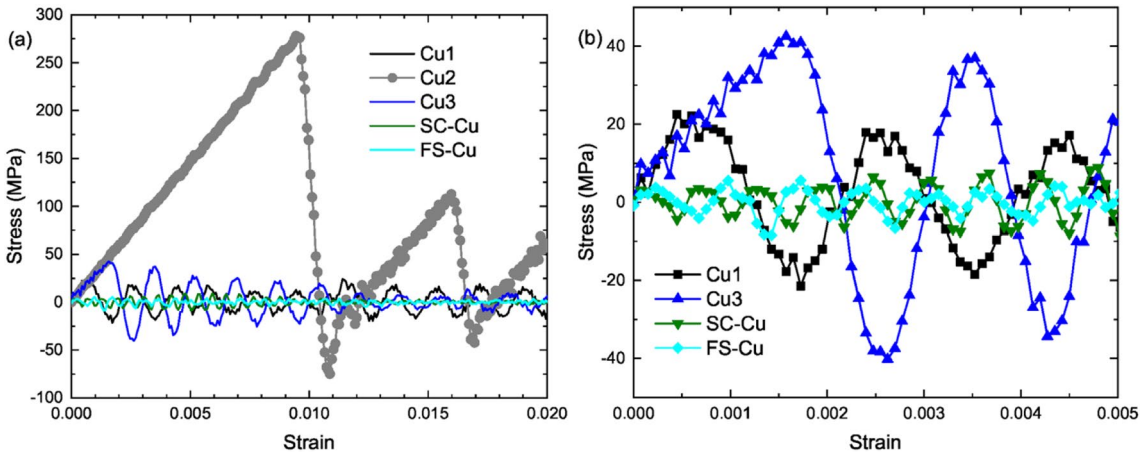

Figure 2: (a) Shear stress–strain curves arising from the glide of an edge dislocation in the Cu layer of a Cu/Cu nanolaminate. The figure compares the response for dislocation glide on planes Cu1, Cu2, and Cu3, the three distinct glide planes in Cu/Cu nanolaminate systems shown in Fig. 1a. For comparison, the response of the same edge dislocation gliding in either Cu single crystal (SC-Cu) or between two free surfaces of the same thickness as the layers in the Cu/Cu nanolaminate (FS-Cu). (b) Zoomed in view of the Cu1, Cu3, SC-Cu, and FS-Cu curves in (a) to better compare their peak stresses.

displacement, and therefore, the dislocation still advances forward, that is, in the direction of the applied shearing.

The oscillatory behavior, involving relatively short backward displacements, is not typically discussed or expected. It can arise from the strong interactions with the defects in the bounding SITB interfaces. Unique to the SITB, the periodicity of the misfit dislocations equals the periodicity of the lattice. The misfit spacing corresponds to the interplanar spacing and so all glide planes in the layer intersect the interface along a misfit dislocation line. Further, the Burgers vectors of the misfit dislocations alternate in sign with every plane, causing the interactions between these misfit dislocation arrays and the moving edge dislocation to change rapidly between attraction and repulsion, resulting in oscillatory glide.

The differences in peak stress to initiate glide on these planes likely arise from differences in their location with respect to the misfit dislocations in the Cu/Cu interface. The interface structures and the dissociated edge dislocation for each plane are shown in Fig. 1 and Fig. S2 in Supplementary Material. As shown, planes Cu1 and Cu3 lie above and below, respectively, plane Cu2, which coincides with the plane on which the b_1 misfit dislocation has extended.

The motion of the edge dislocation **b** on plane Cu2 during the first stages of straining is analyzed in Fig. 3. Before deformation, the edge dislocation has dissociated and its stacking fault can be identified by the hexagonal close-packed (HCP) atom layer marked A. When strain is first applied (Fig. 3b), its leading Shockley partial dislocation on the Cu2 plane begins to transfer to the plane Cu3 below it through a series of reactions. The transfer begins with a reaction between the Shockley partial and a dislocation that emits from one of the interfaces, which produces a leading Shockley partial and second partial dislocation on the Cu3 plane. The latter glides on the Cu3 plane towards the trailing Shockley partial on the Cu2 plane. A similar reaction ensues between it and the trailing Shockley partial, which produces the trailing partial on Cu3. The reaction progresses along the dislocation lines across the layer to the other interface until both the leading and trailing Shockley partials lie fully on the Cu3 plane. The entire transfer requires an increase in the strain and stress (Fig. 3c–e). Once on the Cu3 plane, the full dislocation retains its Burgers vector and creates the same stacking fault marked B as it did on plane Cu2. As shown in Fig. 3f, the size and shape of the stacking fault B resemble those of the initial, strain-free dislocation on plane Cu3 (see Fig. S2(c)). The stress drops once the dislocation glides on plane Cu3. It does not return to plane Cu2 for the remaining straining period. The ultra-high peak stress for plane Cu2, mentioned earlier, corresponds to the stress required to transition the extended dislocation to a parallel plane in order to overcome the extended misfit dislocation.

For comparison, we consider glide of the same dislocation but without the influence of misfit dislocations. In one case, the dislocation is driven to glide in a single crystal without surfaces to confine its motion (SC-Cu) and in another case, it is forced to glide in a thin film between two free surfaces (FS-Cu). Figure 2a shows the shear stress–strain curves for SC-Cu and FS-Cu. The responses are irregular, suggesting that glide is not smooth (Fig. 2b). For the Cu single crystal, the fluctuating response has been reported in previous MD studies [56, 57]. For the SC-Cu and FS-Cu cases here, the first-peak stress amplitudes are much smaller than those in the Cu/Cu nanolaminate, being ~ 4 MPa in the SC and ~ 6 MPa in the FS

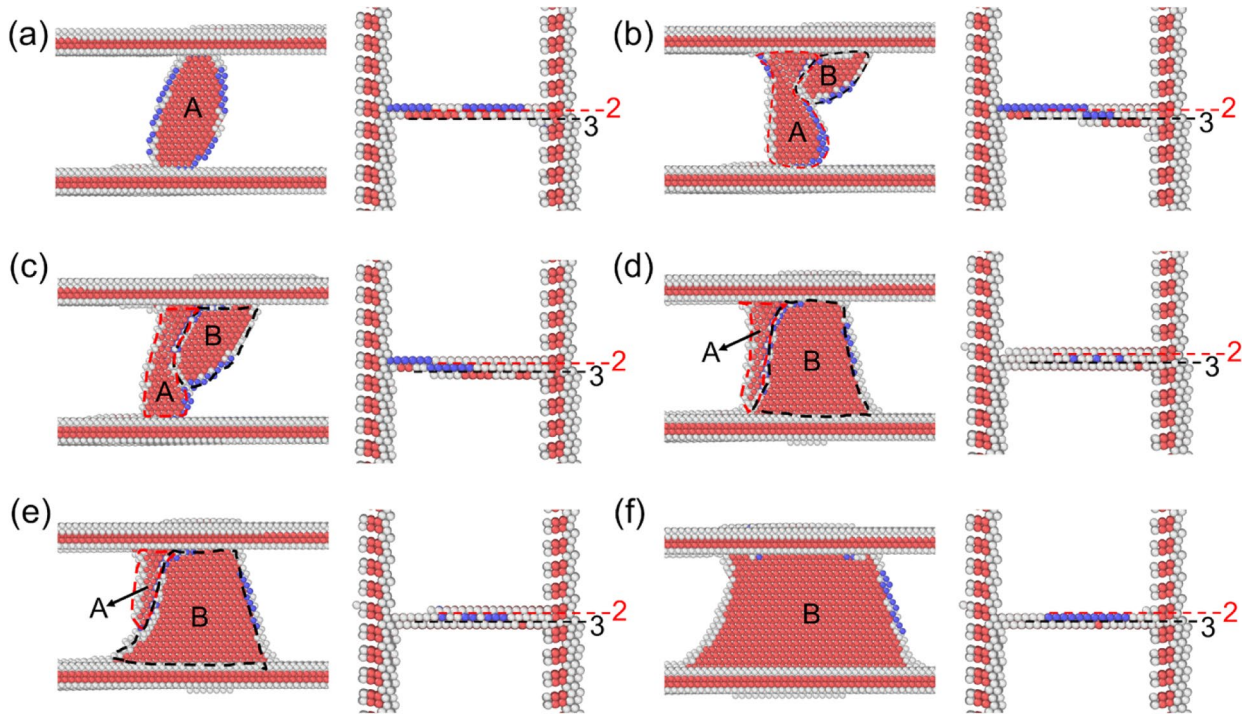

Figure 3: The atomic configurations of the dislocation initially lying on plane 2 at different shear strains: (a) 0 strain, (b) 0.009, (c) 0.0096, (d) 0.00964, (e) 0.009645, and (f) 0.009675. FCC, BCC, HCP atoms, and those with unknown coordination structure are colored by green, blue, red, and gray, respectively. Perfect FCC atoms are deleted to better visualize the interfaces and dislocations. The markers '2' and '3' denote the glide planes 2 and 3 in Fig. 1a, respectively. The labels 'A' and 'B' represent two neighboring atomic layers immediately above planes 2 and 3, respectively. (d) corresponds to the first peak achieved in the stress–strain curve for the dislocation gliding on plane 2.

(Fig. 2b). In the case of the single crystal, the main contribution to resisting motion originates from the lattice. Its peak value can be roughly compared to a Peierls stress calculation for the same dislocation, which we calculate to be ~ 3 MPa, when using the same interatomic potential (see Supplemental Material for details). Note that prior atomistic simulations, which used different model configurations, model sizes, and/or loading modes, reported lower Peierls stresses of an edge dislocation in SC-Cu with the same interatomic potential: 2.5 MPa [58], 1.4 MPa [59], and 1.3 MPa [56]. In the case of FS-Cu, both lattice resistance and confinement imposed by the resisting free surfaces contribute to the dislocation gliding resistance. The result is a nearly twofold increase in resistance from that in the single crystal.

Analysis of the motion in the SC-Cu and FS-Cu cases finds them to be jerky, in which the dislocation repeatedly alternates between accelerating forward and arresting or moving slowly. Unlike CLS in the Cu/Cu laminate, however, they do not oscillate, i.e., do not move backward. In glide, the dislocations in SC or FS are not repeatedly interacting with misfit dislocations with Burgers vectors that alternate repeatedly in sign and are equal or double in value to its Burgers vector.

Nb/Nb nanolaminate

Figure 4 presents the response associated with CLS of an edge dislocation in the Nb/Nb nanolaminate. Unlike the Cu/Cu nanolaminate, dislocations gliding in the Nb layer are constrained to glide between two coherent interfaces. As the stress is applied, dislocations, lying initially on either the Nb1 or Nb2 plane, begin to move when the stress reaches 30 MPa. They remain on their habit planes at all times, and their glide behavior is smooth and not jerky, seemingly unhindered, without being pinned at any point in time. Their corresponding stress–strain responses in Fig. 4 show a continually rising stress as the strain is increased, until reaching a stress plateau of 670–680 MPa. The behavior on the Nb1 and Nb2 planes are similar, likely because the interface structures, where they intersect, are indistinguishable (see Fig. S3(a–b) in Supplementary Material).

To elucidate the role of the interface, deformation simulations are carried out for the same dislocation in SC-Nb and FS-Nb. When the shear strain is first applied, the dislocation in SC-Nb remains immobile until the first-peak stress of 118 MPa is reached. This threshold value is lower than the Peierls stress of the same dislocation, 176 MPa, calculated by molecular statics. Note that prior atomistic simulations, which

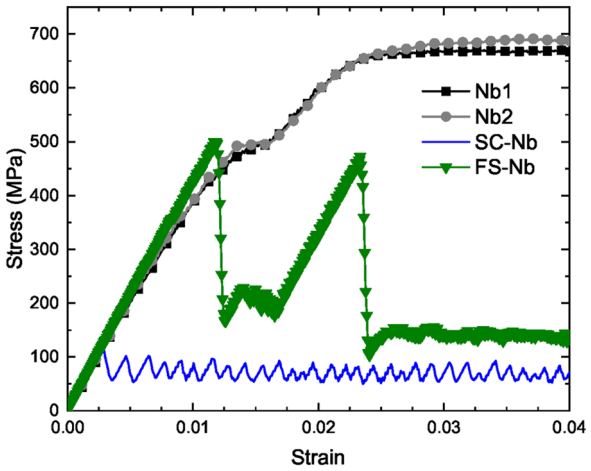

Figure 4: Shear stress–strain curves arising from the glide of an edge dislocation in the Nb layer of an Nb/Nb nanolaminate. The figure compares the response for dislocation glide on plane Nb1 and plane Nb2, the two distinct glide planes in Nb/Nb nanolaminate systems shown in Fig. 1b. For comparison, the response of the same edge dislocation gliding in either Nb single crystal (SC-Nb) or between two free surfaces of the same thickness as the layers in the Nb/Nb nanolaminate (FS-Nb).

used different interatomic potentials [60, 61], reported lower Peierls stresses of an edge dislocation on {110} plane in SC-Nb: 23 MPa [55], 29 MPa [61], and 6 MPa [62]. Once moving, similar to SC-Cu, the stress–strain response associated with the gliding SC-Nb dislocation also fluctuates, but around a positive value of ~ 66 MPa rather than zero. As a result, the dislocation motion is jerky.

In stark contrast with SC-Nb, FS-Nb has three peak stresses in its stress–strain curve, each followed by a substantial drop in stress to a long stress plateau. Dislocation glide is not jerky. In the response, rises in stress are associated with pinning of the dislocation at one of its junctions with the free surface, and drops in stress are associated with depinning. After depinning the third time, the dislocation moves at a constant velocity, no longer held back by the free surfaces. The two major peak stresses (~ 500 MPa and ~ 472 MPa) and steady state stress ~ 144 MPa are significantly larger than the peak stress associated with moving the same dislocation in SC-Nb. As in the case of Cu, the resistance to flow in FS-Nb is twice that in the single crystal, the difference can be attributed to the additional resistance provided by the free surfaces.

CLS in Cu in the Cu/Nb nanolaminate

Next, we examine CLS of the same edge dislocation in a Cu/Nb nanolaminate. The dislocation gliding in the Nb layer and Cu layer is confined by the same incoherent Cu/Nb interface with the same misfit dislocation arrays. The main difference, however, is that the dislocations in one misfit array extend an ISF onto a glide plane of the Cu layer but not the Nb layer.

Figure 5 compares the stress–strain curves associated with dislocation glide on all nine {111} planes in the Cu layer. The responses are irregular, with fluctuating stresses, a sign of jerky flow. They show that glide is highly dependent on which glide plane is used. Among the nine planes, the peak stresses and irregularities are distinct, with no two responses being alike. Glide on the misfit glide planes, Cu5Nb and Cu9Nb, reaches the highest and second highest peak stresses (e.g., first peaks are 316 MPa and 257 MPa), respectively. In contrast, glide on the planes that intersects the interface nearly halfway between two arrays, Cu2Nb and Cu7Nb, results in the lowest peak stresses.

Next, we analyzed the motion of all gliding dislocations under strain. The first-peak stress corresponds to the stress needed to initiate dislocation glide and the stress drop that follows to forward glide. Once in motion, CLS in all planes is jerky, consistent with the irregular stress–strain response. The dislocation arrests causing the stress to rise again until it reaches another peak sufficient to restart CLS. Unlike CLS in the Cu/Cu nanolaminate, CLS in the Cu layer of the Cu/Nb nanolaminate is not oscillatory.

We further examine the incipient motion of the dislocations in the two glide planes that correspond to the misfit dislocations within the interface, since they required substantially higher stresses than the other seven planes. The first of which, Cu5Nb, coincides with the b_1 misfit array. The misfit edge Shockley partial dislocation has extended an ISF from the interface onto Cu5Nb, directly obstructing the glide of the dislocation. When the strain is first applied, the dislocation begins to transfer to Cu6Nb (Fig. 6b), in order to overcome the extended misfit. As the stress and strain increase, the leading Shockley partial gradually moves downward onto the Cu6Nb plane, as indicated by the reduction of the fault A and expansion of fault B (Fig. 6c–e). When the first-peak stress is reached, the dislocation completes its transfer to Cu6Nb, as shown in Fig. 6f, resulting in the first rapid stress drop in Fig. 5a. The shape and width of the dissociated dislocation in Fig. 6f are similar to the stress-free state of the same dislocation initially placed on plane Cu6Nb, as shown in Fig. S4(f). The dislocation then proceeds to glide forward on plane Cu6Nb in a jerky manner. On the other misfit glide plane, Cu9Nb, which coincides with misfit Frank partial b2, the dislocation does not leave its initial glide plane and remains still as the strain is applied. After the first-peak stress is reached, the dislocation begins to move and the stress drops. We show that between the two misfit glide planes, whether or not the misfit protrudes into the layer on the same glide plane as the dislocation can dictate whether or not the dislocation must leave its glide plane or can remain on it.

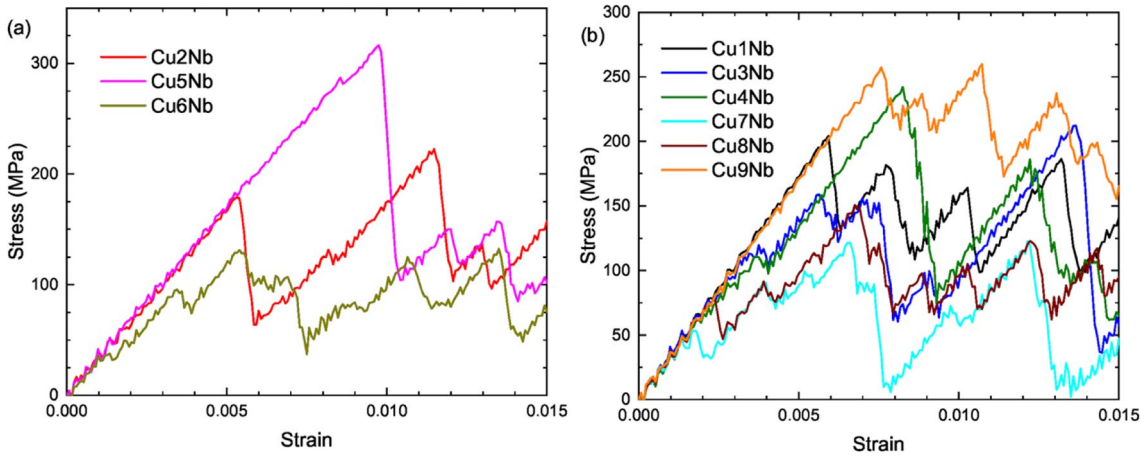

Figure 5: Shear stress–strain curves arising from the glide of an edge dislocation in the Cu layer of a Cu/Nb nanolaminate. (a) compares the responses for dislocation glide on planes Cu2Nb, Cu5Nb, and Cu6Nb, the three distinct glide planes in the Cu/Nb nanolaminate that achieve the relatively higher peak stresses. (b) compares the responses for dislocation glide on the remaining six planes, denoted by Cu1Nb, Cu3Nb, Cu4Nb, Cu7Nb, Cu8Nb, and Cu9Nb. The nine distinct planes, which are marked in Fig. 1c, have different locations with respect to the misfit dislocations lying in the Cu/Nb interface.

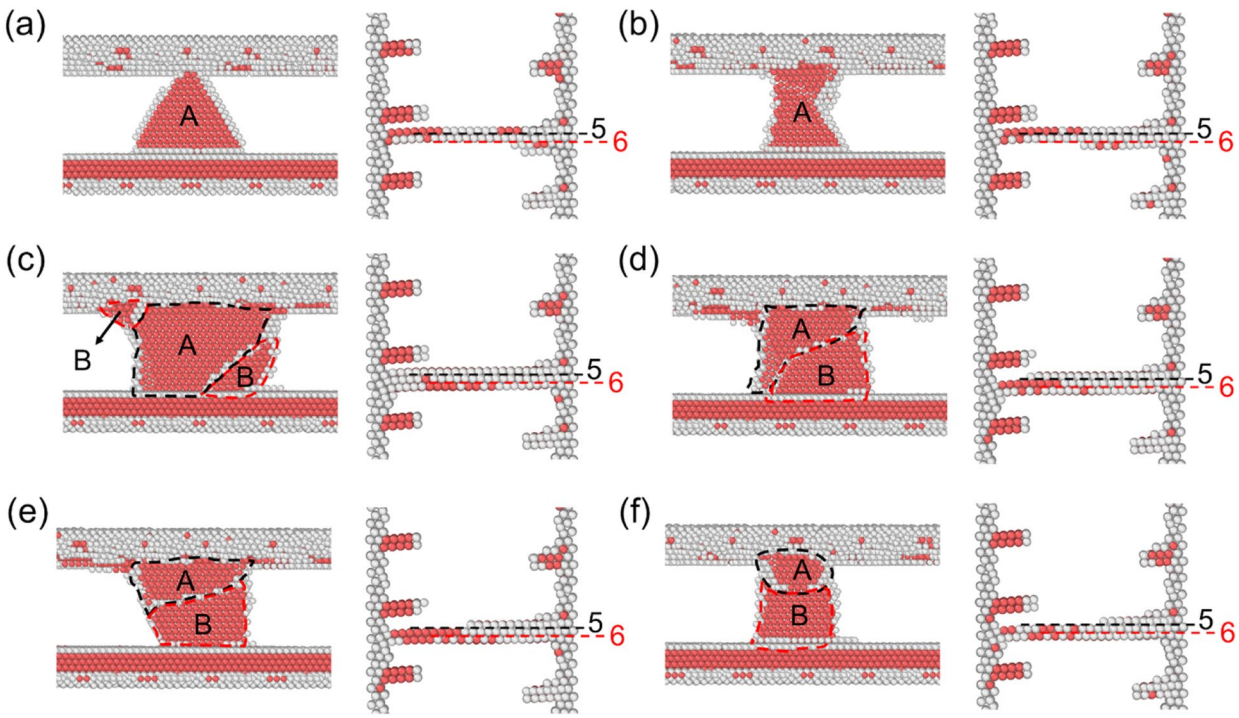

Figure 6: The atomic configurations of the edge dislocation initially lying on plane 5 at different shear strains, starting with (a) 0 strain, when it lies on plane 5, and increasing to (b) 0.0075, (c) 0.00975, (d) 0.00982, (e) 0.00983, and (f) 0.0099. The visualization is the same as that in Fig. 3. The markers '5' and '6' denote glide planes 5 and 6 in Fig. 1c, respectively. The labels 'A' and 'B' represent two neighboring atomic layers immediately above planes 5 and 6, respectively. (c) corresponds to the first peak of stress–strain curve denoted as Cu5Nb in Fig. 5a.

CLS in Nb in the Cu/Nb nanolaminate

Figure 7a and b studies the shear stress–strain curves corresponding to CLS on the eight {110} planes in the Nb layer. The initial atomic configurations of the edge dislocations on each of these planes prior to deformation are shown in Fig. S5 in the supplementary material. Like those for CLS in the neighboring Cu layer, the deformation responses for CLS are irregular and fluctuate, exhibiting many peaks and stress drops. The peak stress levels are on average two to four times higher than those reached in Cu with first-peak stresses ranging from

233 MPa for Nb8Cu to 445 MPa for Nb6Cu. In analyzing dislocation motion in all planes, we find that dislocation remains on its original glide plane and its motion is jerky.

Similar to glide in the Cu layer, the resistance to glide in Nb is greatly affected by the orientation relationship between its glide plane and the Cu/Nb interface misfit dislocations. The two planes experiencing the greatest resistance are the two misfit glide planes, Nb6Cu and Nb3Cu. Dislocations from neither misfit array extend into the Nb layer, possibly explaining why the gliding dislocation can remain on its habit plane at all times. Of the two misfit glide planes, glide on the Nb6Cu plane, which is aligned with the b2 array with the larger Burgers vector, experiences a greater resistance than the Nb3Cu plane, which intersects the b1 array with the smaller Burgers vector. In contrast, the Nb8Cu plane that intersects the interface midway between the b1 and b2 array lines experiences the least resistance. Last, compared to the Cu/Nb nanolaminate, the same Nb dislocation gliding in an Nb/Nb nanolaminate layer bounded by CTBs experiences a much lower resistance to initiate CLS. Glide is smooth and uniform among the planes and not jerky.

Discussion

In this work, we revealed many substantial effects of the atomic structure of the interface on dislocation glide. Simulations of CLS on planes identical in crystallography but distinct in relationship with nearby interface defects suggests that dislocation glide in a nanolaminate will be heterogeneous. Non-uniformity can occur among the layers, with glide in Cu favored over Nb, and within the same layer, for which there is a strong preference for glide on planes that do not intersect with the interface along the lines of misfit dislocations.

In particular, protruding misfit dislocations that dissociate and extend from the interface into the layer on glide planes directly obstruct dislocation motion, forcing the dislocation to overcome it first before proceeding with CLS. In the present study, the misfit extension is a consequence of the low ISF energy of Cu. The implication is that materials with higher ISF energy, such as Al [63], will likely not experience this behavior or vice versa, materials with lower ISF energy, such as Ag [64, 65], Au [66, 67], or FCC multi-principal element alloys [68, 69], can expect local CLS obstruction.

In addition to differences in the critical stress to initiate glide, the hardening behavior as the dislocation glides is also affected. The stress–strain responses for CLS in the layers of the Cu/Nb nanolaminates are irregular, either highly fluctuating or featuring periods of sharp rises in stress followed by rapid drops. We show, however that the jerky manner in which the dislocation moves is not necessarily a consequence of the interface (e.g., dislocation gliding in the Nb layer in Cu/Nb nanolaminate), as the same jerky motion also occurs in the single crystal (e.g., SC-Nb). Yet still, the severity of the stick–slip behavior is enhanced by free surfaces and misfit dislocations in the incoherent interface. The severest irregularity occurs for the Cu/Cu SITB, which is not only the densest with misfit dislocations but the misfits change sign every lattice plane. The resulting motion is slightly oscillatory, and resistance to glide does not increase with straining but softens. The only exception studied here is provided by the coherent interface in Nb, in which first activation of dislocation CLS is the easiest, but the glide resistance increases monotonically as the dislocation moves, until a stress

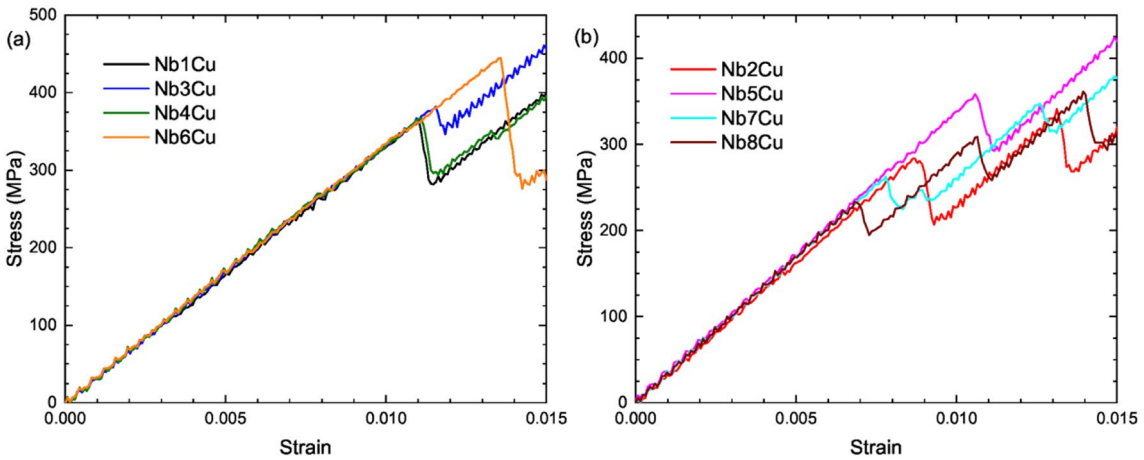

Figure 7: Shear stress–strain curves arising from the glide of an edge dislocation in the Nb layer of a Cu/Nb nanolaminate. (a) compares the responses for dislocation glide on planes Nb1Cu, Nb3Cu, Nb4Cu, and Nb6Cu, the four distinct glide planes in the Cu/Nb nanolaminate that achieve relatively higher peak stresses. (b) compares the responses for dislocation glide on the remaining four planes, denoted by Nb2Cu, Nb5Cu, Nb7Cu, and Nb8Cu. The eight distinct planes, which are marked in Fig. 1d, have different locations with respect to the misfit dislocations lying in the Cu/Nb interface.

plateau is reached. The coherent interface in Nb exhibits the greatest hardening.

Differences in hardening point to need to examine the changes in the dislocation core that is deposited in the boundaries and interfaces as CLS proceeds. Prior atomistic and analytical studies have shown that the changes defects and dislocations experience once they are absorbed into the interface depend sensitively on the chemistry and structure of the interface [14, 25, 27, 31, 70–72]. Surfaces that attract and remove defects deposited from CLS would produce less hardening in CLS than interfaces that diffuse deposited dislocations and even less than coherent interfaces that have little dislocations left in them.

It is worth noting that the stress to nucleate plus glide the dislocation in the layer is much higher than that to move a pre-existing dislocation via CLS. Figure S6 in the supplement presents the shear stress–strain curves for the defect-free Cu/Cu, Cu/Nb and Nb/Nb nanolaminates under shear loading at a constant strain rate of 10^7/s. According to Fig. S6, dislocation nucleation in the laminate without the pre-existing dislocation requires approximately 6 to 10 times higher applied stress than CLS of the pre-existing dislocation in the same laminate. Thus, it is unlikely that additional dislocations will nucleate from the interface, while the dislocation is moving in CLS. In addition, we did not address the effects of changing the layer thickness in this work. In the future, we will quantify those effects on the strength of nanolayered materials when the mechanism for deformation is dislocation glide [73]. The results in the current work, nonetheless, indicate that the glide plane selected for such a size effect study can play a critical role.

Conclusions

In this work, atomistic simulations are performed to investigate the effects of interface morphology on confined layer slip (CLS) in examples of Cu/Cu, Nb/Nb, and Cu/Nb nanolaminates. In all cases, the individual layer thickness was the same value of 5 nm in order to focus on interface structure effects. We show that the interface structure affects the manner in which CLS occurs and the stress required to activate it. The main conclusions are as follows:

- In the Cu/Cu nanolaminate with the symmetric incoherent twin boundary (SITB), CLS is oscillatory, in which the dislocation moves forwards and then backwards repeatedly. Since, in each cycle, the forward distance is significantly larger than the backward one, the dislocation advances forward with straining.
- CLS in the Nb/Nb nanolaminate with a coherent twin boundary is the easiest to activate among all cases, and, unlike dislocation glide in SC-Nb, FS-Nb, or in a composite nanolaminate with a biphase interface, the motion is smooth and the velocity constant. The resistance to motion increases with straining.
- The Cu/Nb nanolaminate has an incoherent {112} Kurdjumov–Sachs interface, which contains misfit dislocation arrays. CLS in the Cu or Nb layer is jerky, in which the dislocation alternates between moving forward and then stopping or slowing down and harder to activate than CLS in the corresponding layer in the single-phase Cu or Nb nanolaminate.
- For the Cu layer in Cu/Nb or Cu/Cu nanolaminate, one misfit dislocation array, among the three, dissociates and extends into the Cu layer on a (111) glide plane. When the moving CLS dislocation coincides with on this glide plane, its motion is initially obstructed. Upon application of the strain, it moves onto the neighboring plane to overcome the extended misfit, an action that requires on average two to ten times more stress than any other glide plane in the layer.

Methodology

Software for atomistic simulations and visualization

LAMMPS [74] is utilized for all atomistic simulations. To visualize the atomic configurations, the adaptive common neighbor analysis [75] implemented in OVITO [76] is employed.

Interatomic potentials

The embedded-atom-method (EAM) potentials developed by Zhang et al. [77] is applied to describe the atomic interactions of Cu–Cu, Nb–Nb, and Cu–Nb. The Cu–Cu and Nb–Nb interactions in this potential are consistent with those in the pure Cu EAM potential by Mishin et al. [78] and pure Nb Finnis–Sinclair potential by Ackland et al. [79]. The Cu EAM potential has been verified capable of simulating dislocation dynamics effectively in Cu [80–83]. The Nb Finnis–Sinclair potential has been utilized in prior work for calculating dislocation-related properties in Nb, such as the Peierls stress [84]. Finally, the Cu–Nb interaction we employ here has been widely applied to understand deformation mechanisms in strained Cu/Nb composites [24, 25, 85, 86].

Bicrystal model set up

Figure 8 shows the schematic that is used for modeling CLS in all nanolaminates considered here. The single crystal layers M and M' have the same layer thicknesses of $L = 5$ nm. The axes x, y, and z denote the lattice coordinates in the layer M, while x', y', and z' are for layer M'. Periodic boundary conditions (PBCs) are applied along the x (or x') and the y (or y') axes, while traction-free boundary conditions are imposed along the z (or z') axis [87, 88]. These boundary condition settings are similar to those used in the periodic array of dislocation model, often applied to calculate the Peierls stress [62, 84] or stress for dislocation glide [57]. The corresponding crystallographic orientations for x (or

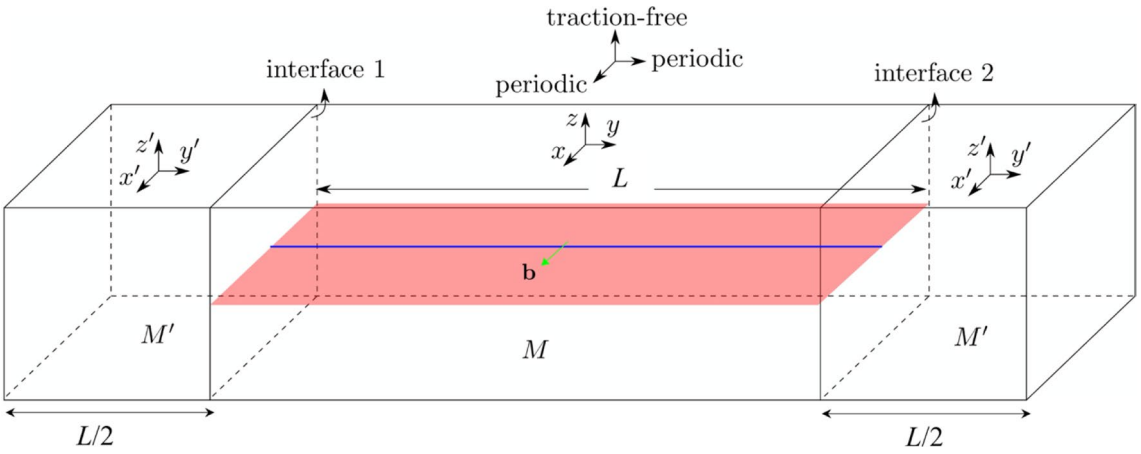

Figure 8: Schematic of the model setup for the periodic cell for the nanolaminate. *M* and *M*′ are two single crystalline layers, dissimilar in orientation and in some cases material. The layer thickness is $L = 5$ nm. The axes *x*, *y*, and *z* correspond to the lattice coordinates in layer *M*, while *x*′, *y*′, and *z*′ are those in layer *M*′. The edge dislocation with the Burgers vector **b** is inserted in the central layer *M*.

x′), *y* (or *y*′), and *z* (or *z*′) are listed in Table 2. The dimensions along *x* (or *x*′), *y* (or *y*′), and *z* (or *z*′) are $43 \times 10 \times 26$ nm^3.

According to the lattice coordinates in *M* and *M*', the interfaces in Cu/Cu, Nb/Nb, and Cu/Nb (or Nb/Cu) nanolaminates are SITBs, CTBs, and {112} KS interfaces, respectively. Grain *M* is shifted in relation to grain *M*' along the two in-plane directions, i.e., *x* (or *x*′) and *z* (or *z*′), to create 100 RBTs, and six different cutoff distances within which one atom is removed from the atom pair in the interface are considered. As a result, a total of 600 initial structures are built for each nanolaminate, and we choose the one with the lowest interface energy after energy minimization by the conjugate gradient algorithm. In each case, the minimization process is terminated when one of the following criteria is satisfied [89, 90]: (1) the energy change between successive iterations divided by the energy magnitude is less than or equal to 10^{-12} or (2) the length of the global force vector for all atoms is less than or equal to 10^{-12} eV/Å.

Single crystal and free surface model set up and boundary conditions

We also studied the glide of an edge dislocation in a single crystal of Cu (SC-Cu), single crystal of Nb (SC-Nb), and between two free surfaces: FS-Cu and FS-Nb. In SC models, PBCs are applied along the x and y axes, while traction-free boundary conditions are imposed along the *z*-axis. In FS models, PBCs are applied along the *x*-axis, while traction-free boundary conditions are imposed along the *y*- and *z*-axes. The dimensions of these four models are the same as the grain *M*, i.e., $43 \times 5 \times 26$ nm^3.

In order for the FS model results to be reliable, it is important to ensure that the interatomic potentials [78, 79] can predict accurate {112} surface energies. We calculate the two surface energies to be 1432 mJ/m^2 and 1962 mJ/m^2, respectively, in Cu and Nb, which are both in reasonable agreement with those from DFT calculations: 1630 mJ/m^2 and 2350 mJ/m^2 [91].

After inserting the dislocation into the bicrystal model, a dynamic relaxation step at 1 K is performed. This low temperature is chosen to minimize the effect of thermal fluctuations. With two vacuum regions created above the top surface and below the bottom surface along the *z*-axis, an NPT ensemble is imposed during thermal relaxation. After relaxation the vacuum regions are removed and the boundary condition along the *z*-axis reverts back to being non-periodic. A similar operation can be found in Ref. [57].

TABLE 2: The lattice coordinates of single crystal lay ers *M* and *M*′ in the nanolaminate systems considered in this work.

Nanolaminate (*M*/*M*′)	*x*	*y*	*z*	*x*′	*y*′	*z*′
Cu/Cu	$[1\bar{1}0]$	$[11\bar{2}]$	[111]	$[1\bar{1}0]$	[112]	$[\bar{1}\bar{1}1]$
Nb/Nb	$[11\bar{1}]$	[112]	$[1\bar{1}0]$	$[\bar{1}\bar{1}1]$	[112]	$[\bar{1}10]$
Cu/Nb	$[1\bar{1}0]$	$[11\bar{2}]$	[111]	$[11\bar{1}]$	[112]	$[1\bar{1}0]$
Nb/Cu	$[11\bar{1}]$	[112]	$[1\bar{1}0]$	$[1\bar{1}0]$	$[11\bar{2}]$	[111]

The axes *x*, *y*, and *z* denote the lattice coordinates in layer *M*, while *x*′, *y*′, and z′ are those for layer *M*′. The dislocation is inserted in the central layer *M*.

Next, the atomic configuration is divided into three regions from the free surface to the glide plane of the dislocation, which are the boundary region, the thermostat region, and the non-thermostat region, in which thicknesses are 1 nm, 4 nm, and 16 nm, respectively. In the thermostat regions, the NVT ensemble is utilized, while in the boundary and non-thermostat regions, the NVE ensemble is applied. The application of the non-thermostat region during dislocation glide on the middle plane leads to the greatest reduction in the artificial friction of thermostat ensemble [92, 93]. The average velocities of the top and bottom boundary regions are independently tailored dynamically using the flexible boundary condition developed by Rodney [94], which ensures the bottom boundary is static, while the top boundary moves at the constant velocity that corresponds to a constant strain rate of 10^7 s^{-1}. During this process, the total forces of boundary regions are zero. More details on the shear loading can be found in Ref. [57]. It should be noted that shear loading in this work is conducted by controlling first the strain rate and then the strain, rather than the load or the stress.

Peierls stress calculations

In the SC models only, we also calculate the Peierls stress by means of the displacement-controlled loading mode used in Refs. [84].

Acknowledgments

W. J. and I. J. B. would like to acknowledge funding from the Office of Naval Research under Grant No. N000141712810. Use was made of computational facilities purchased with funds from the National Science Foundation (CNS-1725797) and administered by the Center for Scientific Computing (CSC). The CSC is supported by the CNSI and the Materials Research Science and Engineering Center (MRSEC; NSF DMR 1720256) at UC Santa Barbara.

Data availability

All data generated or analyzed during this study are included in this published article and its supplementary materials.

Declarations

Conflict of interest The authors declare that they have no conflict of interest.

Supplementary Information

The online version contains supplementary material available at https://doi.org/10.1557/s43578-021-00261-y.

References

1. S. Pathak, N. Velisavljevic, J.K. Baldwin, M. Jain, S. Zheng, N.A. Mara, I.J. Beyerlein, Strong, ductile, and thermally stable bcc-Mg nanolaminates. Sci. Rep. **7**(1), 1 (2017)
2. M. Nasim, Y. Li, M. Wen, C. Wen, A review of high-strength nanolaminates and evaluation of their properties. J. Mater. Sci. Technol. **50**, 215 (2020)
3. M.J. Demkowicz, I.J. Beyerlein, The effects of nanoscale confinement on the behavior of metal laminates. Scr. Mater. **187**, 130 (2020)
4. X. Zhang, E. Fu, N. Li, A. Misra, Y.-Q. Wang, L. Shao, H. Wang, Design of radiation tolerant nanostructured metallic multilayers. J. Eng. Mater. Technol. **134**(4), 041010 (2012)
5. A. Kashinath, A. Misra, M. Demkowicz, Stable storage of helium in nanoscale platelets at semicoherent interfaces. Phys. Rev. Lett. **110**(8), 086101 (2013)
6. N. Li, M.J. Demkowicz, N.A. Mara, Microstructure evolution and mechanical response of nanolaminate composites irradiated with helium at elevated temperatures. JOM **69**(11), 2206 (2017)
7. W. Yang, I.J. Beyerlein, Q. Jin, H. Ge, T. Xiong, L. Yang, J. Pang, Y. Zhou, X. Shao, B. Zhang et al., Strength and ductility of bulk Cu/Nb nanolaminates exposed to extremely high temperatures. Scr. Mater. **166**, 73 (2019)
8. J. Azadmanjiri, C.C. Berndt, J. Wang, A. Kapoor, V.K. Srivastava, C. Wen, A review on hybrid nanolaminate materials synthesized by deposition techniques for energy storage applications. J. Mater. Chem. A **2**(11), 3695 (2014)
9. M. Johnson, P. Bloemen, F. Den Broeder, J. De Vries, Magnetic anisotropy in metallic multilayers. Rep. Prog. Phys. **59**(11), 1409 (1996)
10. P. Ruiz-Díaz, T. Dasa, V. Stepanyuk, Tuning magnetic anisotropy in metallic multilayers by surface charging: an ab initio study. Phys. Rev. Lett. **110**(26), 267203 (2013)
11. E. Fu, A. Misra, H. Wang, L. Shao, X. Zhang, Interface enabled defects reduction in helium ion irradiated Cu/V nanolayers. J. Nucl. Mater. **407**(3), 178 (2010)
12. N. Li, M. Nastasi, A. Misra, Defect structures and hardening mechanisms in high dose helium ion implanted Cu and Cu/Nb multilayer thin films. Int. J. Plast. **32**, 1 (2012)
13. Y. Gao, T. Yang, J. Xue, S. Yan, S. Zhou, Y. Wang, D.T. Kwok, P.K. Chu, Y. Zhang, Radiation tolerance of Cu/W multilayered nanocomposites. J. Nucl. Mater. **413**(1), 11 (2011)
14. M. Wang, I.J. Beyerlein, J. Zhang, W.-Z. Han, Defect-interface interactions in irradiated Cu/Ag nanocomposites. Acta Mater. **160**, 211 (2018)
15. N. Li, J. Carter, A. Misra, L. Shao, H. Wang, X. Zhang, The influence of interfaces on the formation of bubbles in He-ion-irradiated Cu/Mo nanolayers. Philos. Mag. Lett. **91**(1), 18 (2011)

16. J. Wang, A. Misra, An overview of interface-dominated deformation mechanisms in metallic multilayers. Curr. Opin. Solid State Mater. Sci. **15**(1), 20 (2011)
17. I.J. Beyerlein, M.J. Demkowicz, A. Misra, B. Uberuaga, Defect-interface interactions. Prog. Mater. Sci. **74**, 125 (2015)
18. Y. Cui, N. Li, A. Misra, An overview of interface-dominated deformation mechanisms in metallic nanocomposites elucidated using in situ straining in a TEM, J. Mater. Res. **34**(9), 1469 (2019)
19. J. Wang, R. Zhang, C. Zhou, I.J. Beyerlein, A. Misra, Interface dislocation patterns and dislocation nucleation in face-centered-cubic and body-centered-cubic bicrystal interfaces. Int. J. Plast. **53**, 40 (2014)
20. M.J. Demkowicz, J. Wang, R.G. Hoagland, J. Hirth, interfaces between dissimilar crystalline solids, in Dislocations in Solids, vol. 14, ed. by J. Hirth (Elsevier, 2008), pp. 141–207
21. A.P. Sutton, R.W. Balluffi, *Interfaces in Crystalline Materials* (Oxford University Press, Oxford, 1995).
22. R. Zhang, I.J. Beyerlein, S. Zheng, S. Zhang, A. Stukowski, T. Germann, Manipulating dislocation nucleation and shear resistance of bimetal interfaces by atomic steps. Acta Mater. **113**, 194 (2016)
23. K. Kang, J. Wang, S. Zheng, I.J. Beyerlein, Minimum energy structures of faceted, incoherent interfaces. J. Appl. Phys. **112**(7), 073501 (2012)
24. E. Martínez, B.P. Uberuaga, I.J. Beyerlein, Interaction of small mobile stacking fault tetrahedra with free surfaces, dislocations, and interfaces in Cu and Cu-Nb. Phys. Rev. B **93**(5), 054105 (2016)
25. E. Martínez, A. Caro, I.J. Beyerlein, Atomistic modeling of defect-induced plasticity in CuNb nanocomposites. Phys. Rev. B **90**(5), 054103 (2014)
26. I.J. Beyerlein, J. Wang, K. Kang, S. Zheng, N. Mara, Twinnability of bimetal interfaces in nanostructured composites. Mater. Res. Lett. **1**(2), 89 (2013)
27. K. Kang, J. Wang, I.J. Beyerlein, Atomic structure variations of mechanically stable fcc-bcc interfaces. J. Appl. Phys. **111**(5), 053531 (2012)
28. J. Wang, R. Hoagland, X. Liu, A. Misra, The influence of interface shear strength on the glide dislocation–interface interactions. Acta Mater. **59**(8), 3164 (2011)
29. X. Kong, I.J. Beyerlein, Z. Liu, B. Yao, D. Legut, T.C. Germann, R. Zhang, Stronger and more failure-resistant with three-dimensional serrated bimetal interfaces. Acta Mater. **166**, 231 (2019)
30. S. Xu, Y. Li, Y. Chen, Si/Ge (111) semicoherent interfaces: Responses to an in-plane shear and interactions with lattice dislocations. Phys. Status Solidi B **257**, 2000274 (2020)
31. J. Wang, C. Zhou, I.J. Beyerlein, S. Shao, Modeling interface-dominated mechanical behavior of nanolayered crystalline composites. JOM **66**(1), 102 (2014)
32. R. Zhang, T. Germann, X.-Y. Liu, J. Wang, I.J. Beyerlein, Layer size effect on the shock compression behavior of fcc–bcc nanolaminates. Acta Mater. **79**, 74 (2014)
33. W.D. Nix, Mechanical properties of thin films. Metall. Trans. A **20**(11), 2217 (1989)
34. L. Freund, The driving force for glide of a threading dislocation in a strained epitaxial layer on a substrate. J. Mech. Phys. Solids **38**(5), 657 (1990)
35. J. Embury, J. Hirth, On dislocation storage and the mechanical response of fine scale microstructures. Acta Metall. **42**(6), 2051 (1994)
36. N. Li, J. Wang, A. Misra, J.Y. Huang, Direct observations of confined layer slip in Cu/Nb multilayers. Microsc. Microanal. **18**(5), 1155 (2012)
37. P. Anderson, T. Foecke, P. Hazzledine, Dislocation-based deformation mechanisms in metallic nanolaminates. MRS Bull. **24**(2), 27 (1999)
38. A. Misra, J. Hirth, H. Kung, Single-dislocation-based strengthening mechanisms in nanoscale metallic multilayers. Philos. Mag. A **82**(16), 2935 (2002)
39. M. Phillips, B. Clemens, W. Nix, A model for dislocation behavior during deformation of Al/Al3Sc (fcc/L12) metallic multilayers. Acta Mater. **51**(11), 3157 (2003)
40. S. Subedi, I.J. Beyerlein, R. LeSar, A.D. Rollett, Strength of nanoscale metallic multilayers. Scr. Mater. **145**, 132 (2018)
41. A. Misra, J. Hirth, R. Hoagland, Length-scale-dependent deformation mechanisms in incoherent metallic multilayered composites. Acta Mater. **53**(18), 4817 (2005)
42. M. Ardeljan, M. Knezevic, M. Jain, S. Pathak, A. Kumar, N. Li, N.A. Mara, J.K. Baldwin, I.J. Beyerlein, Room temperature deformation mechanisms of Mg/Nb nanolayered composites. J. Mater. Res. **33**(10), 1311 (2018)
43. A. Misra, M. Verdier, Y. Lu, H. Kung, T. Mitchell, M. Nastasi, J. Embury, Structure and mechanical properties of Cu-X (X = Nb, Cr, Ni) nanolayered composites. Scr. Mater. **39**(4–5), 555 (1998)
44. T. Nizolek, M. Begley, R. McCabe, J. Avallone, N.A. Mara, I.J. Beyerlein, T.M. Pollock, Strain fields induced by kink band propagation in Cu-Nb nanolaminate composites. Acta Mater. **133**, 303 (2017)
45. R. Zhang, T. Germann, J. Wang, X.-Y. Liu, I.J. Beyerlein, Role of interface structure on the plastic response of Cu/Nb nanolaminates under shock compression: nonequilibrium molecular dynamics simulations. Scr. Mater. **68**(2), 114 (2013)
46. W. Han, E. Cerreta, N.A. Mara, I.J. Beyerlein, J. Carpenter, S. Zheng, C. Trujillo, P. Dickerson, A. Misra, Deformation and failure of shocked bulk Cu-Nb nanolaminates. Acta Mater. **63**, 150 (2014)
47. X. Zhang, E. Fu, A. Misra, M. Demkowicz, Interface-enabled defect reduction in He ion irradiated metallic multilayers. JOM **62**(12), 75 (2010)

48. M. Zhernenkov, S. Gill, V. Stanic, E. DiMasi, K. Kisslinger, J.K. Baldwin, A. Misra, M. Demkowicz, L. Ecker, Design of radiation resistant metallic multilayers for advanced nuclear systems. Appl. Phys. Lett. **104**(24), 241906 (2014)
49. J. Wang, O. Anderoglu, J.P. Hirth, A. Misra, X. Zhang, Dislocation structures of Σ3 {112} twin boundaries in face centered cubic metals. Appl. Phys. Lett. **95**(2), 021908 (2009)
50. M. Tschopp, D. McDowell, Structures and energies of 3 asymmetric tilt grain boundaries in copper and aluminium. Philos. Mag. **87**(22), 3147 (2007)
51. H. Zheng, X.-G. Li, R. Tran, C. Chen, M. Horton, D. Winston, K.A. Persson, S.P. Ong, Grain boundary properties of elemental metals. Acta Mater. **186**, 40 (2020)
52. M. Demkowicz, L. Thilly, Structure, shear resistance and interaction with point defects of interfaces in Cu-Nb nanocomposites synthesized by severe plastic deformation. Acta Mater. **59**(20), 7744 (2011)
53. M.J. Demkowicz, R.G. Hoagland, Simulations of collision cascades in Cu-Nb layered composites using an EAM interatomic potential. Int. J. Appl. Mech. **01**(03), 421 (2009)
54. S. Xu, E. Hwang, W.-R. Jian, Y. Su, I.J. Beyerlein, Atomistic calculations of the generalized stacking fault energies in two refractory multi-principal element alloys. Intermetallics **124**, 106844 (2020)
55. X. Wang, S. Xu, W.-R. Jian, X.-G. Li, Y. Su, I.J. Beyerlein, Generalized stacking fault energies and peierls stresses in refractory body-centered cubic metals from machine learning-based interatomic potentials. Comput. Mater. Sci. **192**, 110364 (2021)
56. Y. Tang, Uncovering the inertia of dislocation motion and negative mechanical response in crystals. Sci. Rep. **8**(1), 140 (2018)
57. W.-R. Jian, M. Zhang, S. Xu, I.J. Beyerlein, Atomistic simulations of dynamics of an edge dislocation and its interaction with a void in copper: a comparative study. Modell. Simul. Mater. Sci. Eng. **28**(4), 045004 (2020)
58. S. Xu, L. Xiong, Y. Chen, D.L. McDowell, An analysis of key characteristics of the Frank-Read source process in FCC metals. J. Mech. Phys. Solids **96**, 460 (2016)
59. G. Liu, X. Cheng, J. Wang, K. Chen, Y. Shen, Peierls stress in face-centered-cubic metals predicted from an improved semi-discrete variation Peierls-Nabarro model. Scr. Mater. **120**, 94 (2016)
60. D.-Y. Lin, S.S. Wang, D.L. Peng, M. Li, X.D. Hui, An n-body potential for a Zr-Nb system based on the embedded-atom method. J. Phys. **25**(10), 105404 (2013)
61. X.-G. Li, C. Chen, H. Zheng, Y. Zuo, S.P. Ong, Complex strengthening mechanisms in the NbMoTaW multi-principal element alloy, npj Comput. Mater. **6**, 70 (2020)
62. S. Xu, Y. Su, W.-R. Jian, I.J. Beyerlein, Local slip resistances in equal-molar MoNbTi multi-principal element alloy. Acta Mater. **202**, 68 (2021)
63. S. Xu, J.R. Mianroodi, A. Hunter, B. Svendsen, I.J. Beyerlein, Comparative modeling of the disregistry and Peierls stress for dissociated edge and screw dislocations in Al. Int. J. Plast. **129**, 102689 (2020)
64. S. Xu, L. Xiong, Y. Chen, D.L. McDowell, Validation of the concurrent atomistic-continuum method on screw dislocation/stacking fault interactions. Curr. Comput.-Aided Drug Des. **7**(5), 120 (2017)
65. Y. Su, S. Xu, I.J. Beyerlein, Density functional theory calculations of generalized stacking fault energy surfaces for eight face-centered cubic transition metals. J. Appl. Phys. **126**(10), 105112 (2019)
66. S. Xu, M.I. Latypov, Y. Su, Concurrent atomistic-continuum simulations of uniaxial compression of gold nano/submicropillars. Philos. Mag. Lett. **98**(5), 173 (2018)
67. S. Xu, Y. Su, I.J. Beyerlein, Modeling dislocations with arbitrary character angle in face-centered cubic transition metals using the phase-field dislocation dynamics method with full anisotropic elasticity. Mech. Mater. **139**, 103200 (2019)
68. Y. Su, S. Xu, I.J. Beyerlein, Ab initio-informed phase-field modeling of dislocation core structures in equal-molar CoNiRu multi-principal element alloys. Modell. Simul. Mater. Sci. Eng. **27**(8), 084001 (2019)
69. W.-R. Jian, Z. Xie, S. Xu, Y. Su, X. Yao, I.J. Beyerlein, Effects of lattice distortion and chemical short-range order on the mechanisms of deformation in medium entropy alloy CoCrNi. Acta Mater. **199**, 352 (2020)
70. E. Martínez, B.P. Uberuaga, I.J. Beyerlein, Atomic-scale studies of defect interactions with homo-and heterophase interfaces. JOM **68**(6), 1616 (2016)
71. S. Xu, L. Xiong, Y. Chen, D.L. McDowell, Sequential slip transfer of mixed-character dislocations across 3 coherent twin boundary in FCC metals: a concurrent atomistic-continuum study, npj. Comput. Mater. **2**, 15016 (2016)
72. S. Xu, L. Xiong, Y. Chen, D.L. McDowell, Comparing EAM potentials to model slip transfer of sequential mixed character dislocations across two symmetric tilt grain boundaries in Ni. JOM **69**(5), 814 (2017)
73. I.J. Beyerlein, S. Xu, J. Llorca, J.A. El-Awady, J.R. Mianroodi, B. Svendsen, Alloy design for mechanical properties: conquering the length scales. MRS Bull. **44**(4), 257 (2019)
74. S. Plimpton, Fast parallel algorithms for short-range molecular dynamics. J. Comp. Phys. **117**(1), 1 (1995)
75. A. Stukowski, V.V. Bulatov, A. Arsenlis, Automated identification and indexing of dislocations in crystal interfaces. Modell. Simul. Mater. Sci. Eng. **20**(8), 085007 (2012)
76. A. Stukowski, Visualization and analysis of atomistic simulation data with OVITO—the Open Visualization Tool. Modell. Simul. Mater. Sci. Eng. **18**(1), 015012 (2009)

77. L. Zhang, E. Martinez, A. Caro, X.-Y. Liu, M.J. Demkowicz, Liquid-phase thermodynamics and structures in the Cu-Nb binary system. Modell. Simul. Mater. Sci. Eng. **21**(2), 025005 (2013)
78. Y. Mishin, M. Mehl, D. Papaconstantopoulos, A. Voter, J. Kress, Structural stability and lattice defects in copper: ab initio, tight-binding, and embedded-atom calculations. Phys. Rev. B **63**(22), 224106 (2001)
79. G. Ackland, R. Thetford, An improved N-body semi-empirical model for body-centred cubic transition metals. Philos. Mag. A **56**(1), 15 (1987)
80. H. Tsuzuki, P.S. Branicio, J.P. Rino, Molecular dynamics simulation of fast dislocations in copper. Acta Mater. **57**(6), 1843 (2009)
81. Y. Su, S. Xu, On the role of initial void geometry in plastic deformation of metallic thin films: a molecular dynamics study. Mater. Sci. Eng. A **678**, 153 (2016)
82. S. Xu, Y. Su, D. Chen, L. Li, Plastic deformation of Cu single crystals containing an elliptic cylindrical void. Mater. Lett. **193**, 283 (2017)
83. J. Xu, S. Xu, I.J. Beyerlein, Atomistic simulations of dipole tilt wall stability in thin films. Thin Solid Films **689**, 137457 (2019)
84. W.-R. Jian, S. Xu, I.J. Beyerlein, On the significance of model design in atomistic calculations of the Peierls stress in Nb. Comput. Mater. Sci. **188**, 110150 (2021)
85. N. Abdolrahim, H.M. Zbib, D.F. Bahr, Multiscale modeling and simulation of deformation in nanoscale metallic multilayer systems. Int. J. Plast. **52**, 33 (2014)
86. S. Huang, I.J. Beyerlein, C. Zhou, Nanograin size effects on the strength of biphase nanolayered composites. Sci. Rep. **7**, 11251 (2017)
87. S. Xu, Y. Su, Dislocation nucleation from symmetric tilt grain boundaries in bodycentered cubic vanadium. Phys. Lett. A **382**(17), 1185 (2018)
88. D. Chen, S. Xu, Y. Kulkarni, Atomistic mechanism for vacancy-enhanced grain boundary migration. Phys. Rev. Mater. **4**(3), 033602 (2020)
89. S. Xu, J.R. Mianroodi, A. Hunter, I.J. Beyerlein, B. Svendsen, Phase-field-based calculations of the disregistry fields of static extended dislocations in FCC metals. Philos. Mag. **99**(11), 1400 (2019)
90. S. Xu, L. Smith, J.R. Mianroodi, A. Hunter, B. Svendsen, I.J. Beyerlein, A comparison of different continuum approaches in modeling mixed-type dislocations in Al. Modell. Simul. Mater. Sci. Eng. **27**(7), 074004 (2019)
91. R. Tran, Z. Xu, B. Radhakrishnan, D. Winston, W. Sun, K.A. Persson, S.P. Ong, Surface energies of elemental crystals. Sci. Data **3**(1), 160080 (2016)
92. J. Cho, J.-F. Molinari, G. Anciaux, Mobility law of dislocations with several character angles and temperatures in fcc aluminum. Int. J. Plast. **90**, 66 (2017)
93. K. Dang, D. Bamney, K. Bootsita, L. Capolungo, D.E. Spearot, Mobility of dislocations in aluminum: faceting and asymmetry during nanoscale dislocation shear loop expansion. Acta Mater. **168**, 426 (2019)
94. D. Rodney, Activation enthalpy for kink-pair nucleation on dislocations: Comparison between static and dynamic atomic-scale simulations. Phys. Rev. B **76**(14), 144108 (2007)